INTERNATIONAL JOURNAL FOR NUMERICAL METHODS IN FLUIDS
Int. J. Numer. Meth. Fluids 2008; **58**:473–491
Published online 19 February 2008 in Wiley InterScience (www.interscience.wiley.com). DOI: 10.1002/fld.1729

Numerical model for the prediction of dilute, three-dimensional, turbulent fluid–particle flows, using a Lagrangian approach for particle tracking and a CVFEM for the carrier phase

L. A. Oliveira[1,*,†], V. A. F. Costa[2] and B. R. Baliga[3]

[1]*Departamento de Engenharia Mecânica (FCTUC-Polo II), Universidade de Coimbra, 3030-201 Coimbra, Portugal*
[2]*Departamento de Engenharia Mecânica, Universidade de Aveiro, Campus Universitário de Santiago, 3810-193 Aveiro, Portugal*
[3]*Department of Mechanical Engineering, McGill University, 817 Sherbrooke St. West, Montreal, Quebec, Canada H3A 2K6*

SUMMARY

A numerical model for dilute, three-dimensional, turbulent, incompressible fluid–solid particle flows and its application to a demonstration problem are presented. An Eulerian description is used to model the flow of the fluid (carrier) phase, and the governing equations are solved using a control-volume finite element method (CVFEM). The motion of the solid (particulate) phase is simulated using a Lagrangian approach. An efficient algorithm is proposed for locating the particles in the finite element mesh. In the demonstration problem, which involves a particle-laden axisymmetric jet, a modified k–ε turbulence model is used to characterize the velocity and length scales of the turbulent flow of the fluid phase. The effect of turbulence on the particle trajectories is accounted for through a stochastic model. The effect of the particles on the fluid time–mean velocity and turbulence (two-way coupling) is also addressed. Comparisons between predictions and available experimental data for the demonstration problem are presented. Satisfactory agreement is obtained. Copyright © 2008 John Wiley & Sons, Ltd.

Received 21 April 2007; Revised 15 November 2007; Accepted 22 November 2007

KEY WORDS: multiphase flow; particle dispersion; Lagrangian–Eulerian; stochastic approach; CVFEM; CFD; two-way coupling

*Correspondence to: L. A. Oliveira, Departamento de Engenharia Mecânica (FCTUC-Polo II), Universidade de Coimbra, 3030-201 Coimbra, Portugal.
†E-mail: luis.adriano@dem.uc.pt, http://www.dem.uc.pt/

Contract/grant sponsor: Bilateral Franco-Portuguese Cooperation Programme Pessoa 2007/2008, Natural Sciences and Engineering Research Council (NSERC) of Canada

1. INTRODUCTION

Particle dispersion in turbulent flows is encountered in a wide range of engineering applications, including interior dust and particle pollutant control systems, separation processes, pneumatic transport systems, particle combustion in industrial furnaces or energy converters, sediment transport, erosion, some surface treatment procedures and development of new materials, safety and fire suppression systems, and food production processes, among others. In such applications, computational fluid dynamics (CFD) is being increasingly used as an efficient, accessible and affordable way of making numerical predictions in support of design and optimization.

In numerical simulations of fluid–particle flows, the continuous (fluid) phase is typically modeled via an Eulerian approach, while the motion of the dispersed (solid particle) phase is predicted using either a Eulerian or a Lagrangian approach [1–3]. The Lagrangian approach is well suited for the description of the dispersed phase in the so-called *dilute* fluid–particle flows, in which the particle dynamics is controlled primarily by surface and body forces acting on the particle rather than by particle–particle collisions or interactions. The turbulent flow of the continuous (fluid) phase may be represented by two-equation, Reynolds stress, algebraic stress, large eddy simulation (LES), direct numerical simulation, or discrete vortex models, as is discussed in a review by Crowe *et al.* [1]. Because of their relative conceptual simplicity and robustness, the 'standard' and modified versions of the so-called two-equation k–ε and k–ω models have been and still are the most commonly used models for the prediction of industrial turbulent flows [4].

Numerical discretization of the governing differential equations for the continuous phase may be obtained by finite difference, finite volume, or finite element methods [5]. The need to handle irregular geometries has become a requirement today as a consequence of the increasing use of CFD for the solution of real problems, especially in industry. Numerical methods based on structured boundary-fitted orthogonal or non-orthogonal grids are frequently adopted for predicting flows in irregular geometries, with good results [6–9]. However, methods based on finite element meshes have become the methods of choice for the prediction of flows in complex geometries [10–12]). In this work, a control-volume finite element method (CVFEM) is used for the simulation of the continuous phase. CVFEMs combine the merits of well-established finite-volume methods for regular geometries (easy interpretation of the formulation in terms of fluxes, forces, sources; satisfaction of local and global conservation requirements; and efficient techniques for handling the pressure–velocity coupling) and Galerkin finite element methods (geometric flexibility and mathematical models formulated in the Cartesian coordinate system even for complex calculation domains): see, for example, Baliga [13], Ferziger and Peric [5], Mathur and Murthy [14], Baliga and Atabaki [15], and Murthy *et al*. [16] for reviews of CVFEMs, unstructured finite-volume methods, and related topics.

A formulation based on CVFEM for the simulation of the carrier phase in a model for particle dispersion in dilute, two-dimensional, turbulent flows was recently reported by the present authors [17]. In that work, a Lagrangian approach is used to calculate the particle velocities and trajectories. The agreement obtained between predictions and experiments for a plane shear flow test case motivated the extension of the whole procedure to three-dimensional conditions. Preliminary results in that direction were reported in Oliveira *et al.* [18]. Since then, the three-dimensional method has evolved in terms of increased robustness and economy of computer (CPU) time. In particular, an efficient procedure to locate each particle within the Eulerian grid has been introduced with considerable success. This method is reported in the present work, together with the results that were obtained for a demonstration problem consisting of a particle-laden, axisymmetric free jet.

DOI: 10.1002/fld

In the simulations of this demonstration problem, a modified k–ε turbulence model is used to characterize the velocity and length scales of the turbulent flow of the fluid phase. The effect of turbulence on the particle trajectories is accounted for through a stochastic model. The effect of the particles on the fluid time–mean velocity and turbulence (two-way coupling) is also addressed.

2. THE NUMERICAL METHOD

2.1. Mathematical model and CVFEM for prediction of the fluid phase

Following the recommendations of Patankar [19], all the partial differential equations that govern steady three-dimensional turbulent fluid flows and related phenomena occurring in the problems of interest here can be obtained as particular cases of the following general differential equation, written for a unit volume in the conservative form and in Cartesian co-ordinates, x_i, for i ranging from 1 to 3 [20]:

$$\frac{\partial}{\partial x_i}\left(\rho u_i \phi - \Gamma_{\text{eff},\phi}\frac{\partial \phi}{\partial x_i}\right) = S_\phi \tag{1}$$

where the Einstein convention is adopted for the index i. In Equation (1), where the first term inside the brackets accounts for advection, ϕ is a general specific (per unit mass) time-mean, dependent variable, to which are associated particular values or expressions for the corresponding effective diffusion coefficient, $\Gamma_{\text{eff},\phi}$, and source term, S_ϕ. As listed in Table I, the variable ϕ may be interpreted as a velocity component u_i or as unity, in which case Equation (1) represents momentum or mass conservation, respectively, or as a dependent variable associated with the turbulence model employed in this work.

In the simulations of the demonstration problem, the turbulent flow modeling of the fluid phase is based on a modified version of the high-Reynolds number k–ε turbulence model of Launder and Spalding [21], which introduces two additional dependent variables: the turbulence kinetic energy per unit mass, $k = \overline{u_i' u_i'}/2$, and its rate of dissipation, $\varepsilon = (\mu/\rho)\overline{(\partial u_i'/\partial x_j)^2}$, where u_i' is the fluctuating part of the ith velocity component, and ρ and μ stand for the fluid density and dynamic viscosity, respectively. In this work, ρ and μ are assumed to remain constant. The 'turbulent viscosity', μ^{t}, and the energy production term, P_k, appearing in Table I, are defined as $\mu^{\text{t}} = C_\mu \rho k^2/\varepsilon$, $P_k = \mu^{\text{t}}(\partial u_i/\partial x_j + \partial u_j/\partial x_i)\partial u_i/\partial x_j$, respectively ($j$ also ranging from 1 to 3). In turbulent flow configurations where the time-mean vorticity is stretched by the time-mean flow, the same happens to the turbulent vorticity, leading to a reinforcement of the turbulence scale-reduction process. These phenomena, which lead to greater dissipation, less kinetic energy, and lower effective viscosity, are not taken into consideration in the standard k–ε turbulence model mentioned above. As a result, the

Table I. Expressions for $\Gamma_{\text{eff},\phi}$ and S_ϕ in Equation (1).

ϕ	$\Gamma_{\text{eff},\phi}$	S_ϕ
1	0	0
u_i	$\mu+\mu^{\text{t}}$	$-\partial p/\partial x_i + S_{u_i}^{\text{p}}$
k	$\mu+\mu^{\text{t}}/\sigma_k$	$P_k - \rho\varepsilon + S_k^{\text{p}}$
ε	$\mu+\mu^{\text{t}}/\sigma_\varepsilon$	$(C_{1\varepsilon}P_k - C_{2\varepsilon}\rho\varepsilon + C_{3\varepsilon}\rho\chi\varepsilon)\varepsilon/k + S_\varepsilon^{\text{p}}$

DOI: 10.1002/fld

turbulent viscosity predictions yielded by the standard k–ε model for an axisymmetric jet—akin to that considered in the demonstration problem—significantly overestimate its spreading rate. This problem has been addressed by Pope [22], who suggested the inclusion of the vortex stretching effect in the source term of the ε equation (see Table I), by means of a non-dimensional measure of vortex stretching, $\chi = \omega_{ij}\omega_{jk}S_{ki}$, where

$$\omega_{ij} = \frac{1}{2}\frac{k}{\varepsilon}\left(\frac{\partial u_i}{\partial x_j} - \frac{\partial u_j}{\partial x_i}\right) \tag{2a}$$

$$S_{ij} = \frac{1}{2}\frac{k}{\varepsilon}\left(\frac{\partial u_i}{\partial x_j} + \frac{\partial u_j}{\partial x_i}\right) \tag{2b}$$

It should be noted here that when the vorticity vector is not aligned with the time-mean flow (as in planar two-dimensional flows), no vortex stretching occurs and χ correspondingly vanishes.

The terms $S_{u_i}^{\mathrm{p}}$, S_k^{p}, and $S_\varepsilon^{\mathrm{p}}$ in Table I are source contributions from the particle phase: they are defined later in Equations (17), (18a), and (18b), respectively.

The values of the empirical constants in the k–ε turbulence model, $C_\mu, \sigma_k, \sigma_\varepsilon, C_{1\varepsilon}$ and $C_{2\varepsilon}$ are specified in accordance with the recommendations of Launder and Spalding [21] and are listed in Table II. Pope [22] has suggested the value 0.79 for the constant $C_{3\varepsilon}$, and this value is adopted in the present work.

The calculations are not explicitly carried out all the way to solid, impermeable walls. Rather, the wall function approach proposed by Launder and Spalding [21] is adopted in regions immediately adjacent to the wall boundaries of the domain (see also Costa *et al.* [20] and Oliveira *et al.* [17] for details). Zero-normal-gradient conditions are assumed to hold at outflow boundaries of the calculation domain [19], and prescribed values are used for the dependent variables at inlet boundaries.

The equations that govern the fluid phase (all specialized forms of Equation (1)) are numerically integrated by using a CVFEM, reviewed by Baliga [13], with a mass-weighted scheme for discretization of the advection terms. The calculation domain is first discretized into eight-node bricks, and then each brick is divided into six four-node tetrahedral finite elements, as illustrated schematically in Figure 1.

Owing to the planar character of the brick surfaces, in the proposed discretization, curved boundaries are approximated as piecewise-planar surfaces. The midpoints of each element edges are identified as points A–F in Figure 1(c). To build a control volume around each of the nodes, such as 1–4 in Figure 1(c), the midpoints are joined as shown in the figure, thus forming three plane control sub-surfaces, two of which are triangular and one is quadrilateral. These three control sub-surfaces define four control sub-volumes in the tetrahedral element, each one associated with a node of the element. When all the bricks are assembled, the control sub-surfaces and sub-volumes are also assembled to form a closed control surface around each internal node of the domain, thus defining a control volume associated with it.

Table II. Values assigned to the empirical constants in the standard k–ε turbulence model.

C_μ	σ_k	σ_ε	$C_{1\varepsilon}$	$C_{2\varepsilon}$
0.09	1.0	1.3	1.44	1.92

DOI: 10.1002/fld

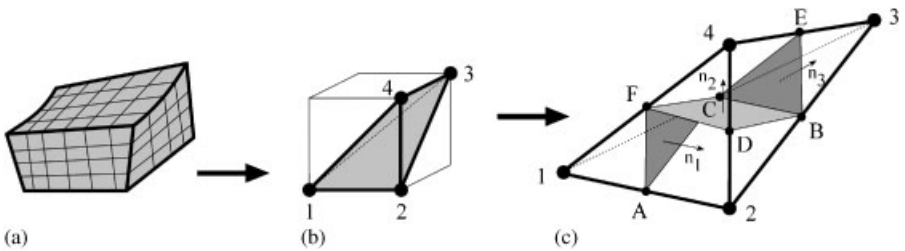

Figure 1. Domain discretization: (a) division into bricks; (b) brick division into tetrahedral elements; and (c) a four-node tetrahedral element.

2.2. *Lagrangian tracking procedure for the particle phase*

The solid phase is assumed to be composed of hard, spherical, non-rotating, smooth, elastic particles of uniform diameter d^{p}, mass m^{p}, and mass density ρ^{p}, where the superscript, p, is used to identify the particulate phase. In the problems considered here, the focus is on gas–solid particle flows, and the only significant forces acting on each particle are assumed to be the drag, gravitational, and local pressure gradient forces. The equation of motion of a single particle of unit mass is thus reduced to the following form [23]:

$$\frac{\mathrm{d}u_i^{\mathrm{p}}}{\mathrm{d}t}=\frac{3}{4}\frac{\mu}{\rho^{\mathrm{p}}(d^{\mathrm{p}})^2}C_{\mathrm{D}}\,Re^{\mathrm{p}}(u_i-u_i^{\mathrm{p}})+g_i\left(1-\frac{\rho}{\rho^{\mathrm{p}}}\right)-\frac{1}{\rho^{\mathrm{p}}}\frac{\partial p}{\partial x_i} \tag{3}$$

where the three terms of the right-hand side represent, in the same order, the forces that were mentioned above and are responsible for the particle acceleration (left-hand side). In Equation (3), the particle Reynolds number, Re^{p}, is based upon the relative velocity

$$|\mathbf{V}^{\mathrm{rel}}|=\sqrt{(u_i-u_i^{\mathrm{p}})^2}$$

and its product with the drag coefficient C_{D} is calculated here using the following empirical relation [24]:

$$C_{\mathrm{D}}Re^{\mathrm{p}}=\begin{cases}24+3.6(Re^{\mathrm{p}})^{0.687} & (Re^{\mathrm{p}}\leqslant 1000)\\ 0.44\,Re^{\mathrm{p}} & (Re^{\mathrm{p}}>1000)\end{cases} \tag{4}$$

The particle trajectories, x_i^{p}, are related to their instantaneous velocities by the following equation:

$$\frac{\mathrm{d}x_i^{\mathrm{p}}}{\mathrm{d}t}=u_i^{\mathrm{p}} \tag{5}$$

The position and velocity of each particle along its trajectory are calculated for a time level $t+\Delta t$, as functions of the corresponding values that are available for the previous time level, t. Equations (3) and (5) can be solved analytically, provided Δt is small enough, so that the properties of the fluid phase may be considered essentially unchanged between the instants t and $t+\Delta t$. In this case, Equation (3) has the linear form:

$$\frac{\mathrm{d}u_i^{\mathrm{p}}}{\mathrm{d}t}=A-Bu_i^{\mathrm{p}} \tag{6}$$

DOI: 10.1002/fld

where A and B are both constants over the time step of interest. The analytical solution for a time step Δt is thus

$$u_i^{\mathrm{p}} = u_{0i}^{\mathrm{p}}\, \mathrm{e}^{-B\Delta t} + \frac{A}{B}(1-\mathrm{e}^{-B\Delta t}) \tag{7}$$

from which the position of the particle can be obtained through Equation (5), yielding

$$x_i^{\mathrm{p}} = x_{0i}^{\mathrm{p}} + \frac{A}{B}\Delta t + \frac{1}{B}\left(x_{0i}^{\mathrm{p}} - \frac{A}{B}\right)(1-\mathrm{e}^{-B\Delta t}) \tag{8}$$

where the subscript '0' indicates the initial value for the time integration.

As an alternative to the above-mentioned analytical solution, for those cases where the fluid properties cannot be considered constant over the integration time interval, Δt, the present model also includes a fourth-order Runge–Kutta numerical integration scheme. The corresponding details may be found in Oliveira [25].

The selection of the time step, Δt, is based on the local value of the Stokes number, $St = \tau^{\mathrm{p}}/\tau$, where τ^{p} and τ are the characteristic particle and fluid response times, respectively. The expression for τ^{p} is [25]

$$\tau^{\mathrm{p}} = -\tau^s \ln\left[1 - \frac{(1-\mathrm{e}^{-1})/\tau_s}{1/\tau_s + K_0}\right] \tag{9}$$

where τ^s is a response time when only drag forces act upon the particle [25]:

$$\tau^s = \frac{4}{3}\frac{\rho^{\mathrm{p}}(d^{\mathrm{p}})^2}{\mu}(C_{\mathrm{D}}Re^{\mathrm{p}})^{-1} \tag{10}$$

and $K_0 = \sum |\mathbf{F}/m^{\mathrm{p}}|/\sqrt{u_i^2}$ is a correction factor that accounts for the remaining forces $\mathbf{F}$—pressure and gravity, in the present case. The fluid response time, τ, is defined as

$$\tau = \delta/\sqrt{u_i^2} \tag{11}$$

where δ is a characteristic dimension of the Eulerian grid (here taken as the volume of the CVFEM mesh element within which the particle is localized at instant t, divided by its external surface area). In practice, if $St \ll 1$, the particle essentially follows the fluid flow, and the time step is set as $\Delta t = \tau$; if $St \approx 1$ or $St \gg 1$, then $\Delta t = \tau^{\mathrm{p}}$. In any case, Δt should not significantly exceed the time necessary for the particle to traverse the local Eulerian grid cell. A further restriction is imposed for those cases where the Runge–Kutta method is used: Δt should always be kept below the stability limit that applies to this method.

In Equation (3), the computation of the fluid forces that are responsible for particle motion requires the determination of the CVFEM mesh element in which the particle is located at each Lagrangian time level, t. Analytical or tabular look-up expressions may be used for this purpose in structured meshes with Cartesian (rectangular parallelepiped) elements, but this approach does not apply to computational meshes composed of tetrahedral elements, such as the one shown in Figure 1(c). However, the particle location can be easily determined by using a simple geometrical argument: let $\mathbf{r}_j$ be the vector directed from the instantaneous location of the particle, $\mathbf{x}^{\mathrm{p}}$, to the geometrical center of any one of the four external surfaces of a tetrahedral finite element, and let $\hat{n}_j$

DOI: 10.1002/fld

be the outward-pointing unit normal to that surface ($j=1$ to 4); if the inner product $a_j=(\mathbf{r}_j\cdot\hat{n}_j)$—the Einstein index notation is not used here—is non-negative for *all* the element external surfaces ($j=1$ to 4), then the particle is located inside that element or at one of its four surface boundaries. In order to minimize the use of time consuming 'if' statements in the corresponding computer code, an integer I_j is first defined for each of the four external surfaces of a tetrahedral element through the use of the FORTRAN Sign function, such that

$$I_j=\text{Sign}[1,a_j]=1 \quad \text{if } a_j\geqslant 0 \tag{12a}$$

$$I_j=\text{Sign}[1,a_j]=-1 \quad \text{if } a_j<0 \tag{12b}$$

Using these integers, I_j, it can be concluded that the particle lies inside the element if $\sum_{j=1}^{4} I_j=4$. The local fluid velocity and pressure gradient are then calculated by linear interpolation of the corresponding values already available at the four nodes of the tetrahedral element. However, prior to this localizing procedure, one must search throughout the computational domain (Figure 1(a)) to find the hexahedron (Figure 1(b)) that contains the tetrahedron (Figure 1(c)) within which the particle lies. For three-dimensional conditions, optimization of this searching procedure becomes a crucial need in order to keep the computer (CPU) time required for particle tracking within reasonable limits. Several criteria may be used, ranging from the 'blind search' (check every hexahedron within the whole domain) to a 'circular search' (look up around the last particle location) or to a search based on both the last particle location and the fluid velocity at that position: the last of these options performs the best, but some uncertainty remains in highly recirculating flows or simply due to the stochastic nature of the turbulent velocity fluctuations (as in the present conditions). To overcome such difficulties, in this work, the basic ideas of the 'optimal search' described by Chen [26] for two-dimensional, body-fitted coordinates were adapted to the present three-dimensional, CVFEM grid structure.

Again, let $\mathbf{r}_j$ be the vector directed from the instantaneous location of the particle, $\mathbf{x}^{\mathrm{p}}$, to the geometrical center of any one of the six external surfaces of the hexahedron shown in Figure 2, and let $\hat{n}_j$ be the external unit normal to that surface ($j=e,w,n,s,u,d$). Again, curved boundary surfaces of the calculation domain are treated as piecewise-planar surfaces. If the inner product $(\mathbf{r}_j\cdot\hat{n}_j)$—again, the Einstein index notation is not used here—is non-negative for *all* the six hexahedral external surfaces ($j=e,w,n,s,u,d$), then the particle is located inside that hexahedron or at one of its six surface boundaries. The search is then extended to all the six tetrahedral elements within that hexahedron, as described above, until the particle-containing element is found. Now, if the particle is located outside the hexahedron, a search path must be established to localize the particle-containing hexahedron. If, for instance, the particle is located eastwards relative to the e

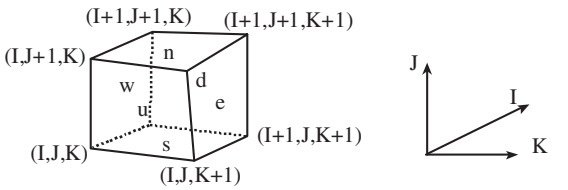

Figure 2. Vertices, surfaces (e,w,n,s,u,d), and grid indices (I,J,K) of a single hexahedron of the three-dimensional mesh. Each hexahedron is identified in the domain by its south-west vertex of indices (I,J,K).

DOI: 10.1002/fld

surface of the hexahedron in Figure 2, then $I_e = -1$ and $I_w = 1$, with I_e and I_w defined as in Equation (12a), (12b). In this case, a K index increment in the search path, ΔK, defined as

$$\Delta K = \frac{1 - I_e}{2} - \frac{1 - I_w}{2} \tag{13a}$$

would give $\Delta K = 1$, thus meaning that the search should proceed eastwards. The same reasoning applies to the index increments ΔI and ΔJ, according to the definitions:

$$\Delta I = \frac{1 - I_d}{2} - \frac{1 - I_u}{2} \tag{13b}$$

$$\Delta J = \frac{1 - I_n}{2} - \frac{1 - I_s}{2} \tag{13c}$$

In summary, if the last inspected hexahedron is identified by the node $(I_{\text{old}}, J_{\text{old}}, K_{\text{old}})$ and the particle does not lie inside it, then the search should proceed towards the hexahedron of indices $I_{\text{new}} = I_{\text{old}} + \Delta I$, $J_{\text{new}} = J_{\text{old}} + \Delta J$, $K_{\text{new}} = K_{\text{old}} + \Delta K$. This procedure is repeated until the particle-containing hexahedron is eventually found.

Geometrical reasoning is also used to determine the residence time or the time spent by the particle in each tetrahedral element it crosses. This is necessary for an averaging procedure and also to account for two-way coupling effects, as will be seen later. The interactions of the particles with solid boundaries are modeled through elastic collisions or with the introduction of a restitution coefficient. For each particle, the trajectory calculation is terminated when the particle leaves the calculation domain at outflow boundaries, or, alternatively, its position remains unchanged after a significant amount of time.

In this work, the effect of fluid turbulence upon particle dispersion is accounted for using the concept of particle–eddy encounters [27]. The instantaneous fluid velocity components to be used in Equation (3) are estimated by superimposing, on the corresponding time-mean values, fluctuating components u_i' that are obtained by randomly sampling a Gaussian distribution with standard deviation $(2k/3)^{0.5}$:

$$u_i' = \sqrt{2k/3}\,\zeta_i \tag{14}$$

where ζ_i $(i = 1, 2, 3)$ are three independent random variables with zero mean and unit variance. The time duration of particle–eddy interaction is estimated as the minimum of two time scales, namely, an eddy transit time, t_e, and an eddy lifetime, t_r:

$$t_e = \frac{\ell_e}{\sqrt{2k/3}} \tag{15a}$$

$$t_r = -\tau^{\text{p}} \ln\left(1 - \frac{\ell_e}{\tau^{\text{p}} |\mathbf{V}^{\text{rel}}|}\right) \tag{15b}$$

$$\ell_e = \frac{C_\mu^{0.75} k^{1.5}}{\varepsilon} \tag{15c}$$

where ℓ_e stands for the characteristic length scale of the randomly sampled eddy. This interaction time should never be exceeded by the Lagrangian time step, Δt, used in the determination of the particle trajectory. The instantaneous fluid velocities are updated every time the particle encounters a new eddy.

DOI: 10.1002/fld

2.3. Eulerian–Lagrangian modeling of the particle-laden flow

Two-way coupling effects are included in this model through the particle–source–in cell strategy of Crowe *et al.* [28]. The global calculation procedure may be described as follows: first, the fluid flow is predicted ignoring the presence of particles; these fluid flow results are then frozen and all particle trajectories calculated, thus leading to the determination of momentum and turbulent energy source (or sink) contributions for each control volume that has been visited by all particles along their paths; with these new source terms, the CVFEM calculations are redone for the fluid flow; then the former particle trajectories are corrected; and the whole procedure is repeated until convergence is achieved.

Along its own trajectory, a particle with mass m^{p} is actually representative of a number of analogous particles introduced in the domain at a rate $\dot{N}$ through the same injection point. Each trajectory j is associated with a particle mass flow rate $\dot{m}_j^{\mathrm{p}} = \dot{N}_j m^{\mathrm{p}}$. As it crosses an Eulerian cell of volume Δv, a momentum source contribution is generated for the continuous phase [28, 29]:

$$(S_{u_i}^{\mathrm{p}})_j \Delta v = -\dot{m}_j^{\mathrm{p}}[(u_i^{\mathrm{p}})_{\mathrm{out}} - (u_i^{\mathrm{p}})_{\mathrm{in}}] + \dot{m}_j^{\mathrm{p}}(t_{\mathrm{out}} - t_{\mathrm{in}}) \left[g_i \left(1 - \frac{\rho}{\rho^{\mathrm{p}}}\right) - \frac{1}{\rho^{\mathrm{p}}} \frac{\partial p}{\partial x_i} \right] \tag{16}$$

Equation (16) shows that the particle momentum source term is composed of two parts: the change of momentum of the particles (net efflux of particle momentum) and the influence of the external forces (gravity and local pressure gradient) acting on the particles. In this equation, g_i is the gravity acceleration component along the direction i, and the indices 'in' and 'out' refer to the particle entering and leaving the control volume, respectively. If any particular control volume is traversed by a number of trajectories, T_j, the resulting source contribution from the particle phase to the source term S_{u_i} in Equation (1) (with $\phi \equiv u_i$) becomes

$$S_{u_i}^{\mathrm{p}} = \sum_{j=1}^{Tj} (S_{u_i}^{\mathrm{p}})_j \tag{17}$$

Analogously, and following Gouesbet *et al.* [30], the influence of the particles upon the turbulence level of the carrier phase (turbulence modulation) is accounted for by including the corresponding source term contributions in Equation (1) (with $\phi \equiv k, \varepsilon$):

$$S_k^{\mathrm{p}} = \overline{u_i S_{u_i}^{\mathrm{p}}} - \overline{u_i}\,\overline{S_{u_i}^{\mathrm{p}}} \tag{18a}$$

$$S_\varepsilon^{\mathrm{p}} = 1.1 \frac{\varepsilon}{k} S_k^{\mathrm{p}} \tag{18b}$$

where the time averages are computed for all the trajectories crossing the Eulerian control volume. In each Eulerian cell of volume Δv, crossed by a number T_j of particle trajectories, a particle volume fraction, α, is defined by

$$\alpha = \frac{\sum_{j=1}^{T_j} \dot{N}_j (t_{\mathrm{out}} - t_{\mathrm{in}})_j \pi (d^{\mathrm{p}})^3 / 6}{\Delta v} \tag{19}$$

where $\dot{N}_j$ is the number of particles per unit time that cross the cell along trajectory j, and $(t_{\mathrm{out}} - t_{\mathrm{in}})$ is the time each of these particles takes to traverse the cell. Correspondingly, the ensemble-averaged

DOI: 10.1002/fld

particle velocities, $\langle u_i^{\mathrm{p}} \rangle$, in each Eulerian control volume, are computed by

$$\langle u_i^{\mathrm{p}} \rangle = \frac{\sum_{j=1}^{T_j} \dot{N}_j (t_{\mathrm{out}} - t_{\mathrm{in}})_j (u_i^{\mathrm{p}})_j}{\sum_{j=1}^{T_j} \dot{N}_j (t_{\mathrm{out}} - t_{\mathrm{in}})_j} \tag{20}$$

where $(u_i^{\mathrm{p}})_j$ is the ith component of the local, instantaneous velocity of a particle along trajectory j.

3. RESULTS

The CVFEM used for the simulations of the fluid flow in the present three-dimensional calculations has been thoroughly reported, tested, and validated in a previous paper by Costa *et al.* [20]. Several preliminary tests of this CVFEM along with the aforementioned formulations for the simulations of the fluid–solid particle flows were conducted prior to their application to the test problem described later in this section. Analytical solutions to some forms of the particle flow equations, namely, Equations (3) and (5), allowed some rudimentary verifications, such as the flow of a tracer particle or the matching of the analytical expression for particle terminal velocity in the Stokes regime [$Re^{\mathrm{p}} \approx O(1)$] in uniform flow fields. Such tests were used to check the alternative (numerical) Runge–Kutta integration procedure. The corresponding results did match the analytical ones within the computer round-off precision. Preliminary tests of the two-way coupling procedure were also performed by observing, in a Poiseuille-type flow of air within a pipe, the variation of the pressure drop as a function of concentration of the solid particles, which were evenly injected at the pipe inlet section: as expected, a nearly linear dependence was predicted; Additional details are available in Oliveira *et al*. [17].

After the completion of the above-mentioned tests successfully, the proposed method was used to simulate a turbulent axisymmetric air jet laden with solid particles. This problem was chosen as the test case for demonstrating the proposed method because the results could be compared with experimental data available in the published literature. The test problem is essentially two dimensional if the mathematical model is expressed in a cylindrical (x, θ, r) coordinate system. However, when the mathematical model is described with respect to a Cartesian coordinate system (x, y, z), as in the present work, the test problem is actually three dimensional and it can be used to conveniently demonstrate the capabilities of the proposed three-dimensional CVFEM-based procedure. Details of the experimental setup and inlet conditions for both the fluid and the solid particulate phases are thoroughly reported in the experimental paper of Modarress *et al.* [31] and also in the numerical study of Elghobashi *et al.* [32]. In their experiments, Modarress *et al.* [31] used a two-color, frequency-shifted laser Doppler anemometer (LDA) to perform the velocity measurements for the fluid and the particle phases. At each location, the (time-mean and fluctuating) axial and radial velocity components of each phase were measured separately. By lowering the sensitivity of the LDA system to the seeding particles (micron-sized alumina tracer particles that were necessary for the continuous-phase velocity measurements), only the light scattered from the larger particles (dispersed phase) was processed. For the gas-phase measurements in the presence of solid particles, the signals from the dispersed phase were identified (through their larger signal amplitude, compared with that of the seeding particles) and then rejected. These experimental data have been used in earlier investigations to check two-phase gas–particle flow predictions [32–34].

DOI: 10.1002/fld

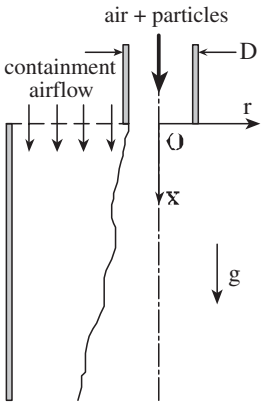

Figure 3. Schematic representation of the turbulent jet of air and solid particles [31].

A schematic representation of the turbulent jet of air and solid particles investigated in the experiments of Modarress *et al.* [31] is shown in Figure 3. This two-phase jet issues downwards from a tube of inner diameter $D=20\,\text{mm}$, with inlet power-law time-mean velocity profile and turbulence intensity given by

$$u_x/u_{x,c}=[1-(2r/D)]^{1/n} \tag{21a}$$

$$\sqrt{\frac{1}{3}\overline{u_i'^2}}/u_{x,c}=0.04+0.1\,\frac{r}{D} \tag{21b}$$

respectively, where r is the radial position, $u_{x,c}=13.4\,\text{m/s}$ is the centerline air velocity and $n=6.6$. The air jet [$\rho=1.178\,\text{kg/m}^3$, $\mu=1.806\times10^{-5}\,\text{kg/(m.s)}$] is laden with uniform-size glass beads ($\rho^{\text{p}}=2990\,\text{kg/m}^3$, $d^{\text{p}}=200\,\mu\text{m}$) that are injected at a mass flow rate $\dot{m}^{\text{p}}=3.2\times10^{-3}\,\text{kg/s}$, with a centerline particle velocity of $u^{\text{p}}_{x,c}=10.2\,\text{m/s}$ and a power-law velocity profile with exponent $n=27.6$. The particle-laden air jet is discharged into a co-flowing low-velocity air stream. This co-flowing containment flow has a time-mean velocity of $0.05\,\text{m/s}$ and turbulence intensity of 0.1. It surrounds the air jet and extends to a cylindrical container wall ($30\,D$ in diameter, $90\,D$ long). Most of the experimental data provided by Modarress *et al.* [31] were obtained through measurements performed at the $x/D=20$ longitudinal stage. The present predictions for this demonstration problem are thus restricted to the two-phase jet sub-region defined by the longitudinal extent $0\leqslant x/D\leqslant20$. A systematic analysis was conducted in order to establish the radial and longitudinal dimensions of the calculation domain that albeit smaller than the ones in the experimental test rig still ensured that the domain boundary conditions did not interfere with the particle-laden jet predictions obtained for $0\leqslant x/D\leqslant20$. This analysis led to the conclusion that, for the present specific purposes, it is sufficient to locate the radial and longitudinal domain boundaries at $2r=15\,D$ and $x=50\,D$, respectively. These dimensions of the calculation domain were thus adopted in the final numerical simulations.

The three-dimensional Eulerian mesh that was used to discretize the cylindrical calculation domain for the numerical simulations of the demonstration problem is illustrated in Figure 4. As a first step to build this mesh, a two-dimensional, uniformly spaced grid was defined at $x=0$. This grid spans the cross section of the cylindrical container of diameter $15\,D$. For this purpose, the

DOI: 10.1002/fld

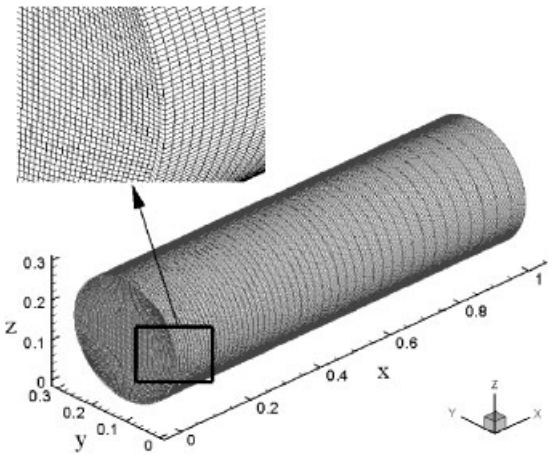

Figure 4. Details of the grid used in the numerical simulations.

perimeter of the circular outer boundary of the cross section at $x=0$ was first divided into four equal sections; nodes were uniformly distributed in each of these sections; the internal nodes were then evenly distributed along lines connecting corresponding boundary nodes on opposite sections of the perimeter. Finally, the three-dimensional grid was generated by 'extruding' the aforementioned two-dimensional grid along the x-axis. The resulting three-dimensional grid is gradually expanded along the longitudinal, main flow direction, x (see Figure 4). The radial coordinate at any position defined by the Cartesian coordinates (x, y, z) is thus $r=[(y-y_c)^2+(z-z_c)^2]^{1/2}$, where y_c and z_c are the y and z values at the centerline of the cylindrical flow domain.

Grid dependence tests were conducted using (x, y, z) Eulerian meshes with $31\times45\times45$, $41\times55\times55$, and $51\times65\times65$ nodes. A sample of the results yielded by these tests is shown in Figure 5, where single-phase (no particle-laden) predictions of the radial profile of the normalized time-mean fluid velocity obtained using each of the aforementioned grids are presented. On the basis of such results, it was concluded that approximate grid independence is ensured with the $51\times65\times65$ mesh, which was thus adopted for the remaining calculations.

The Lagrangian predictions were based on tracking a number T_j of particle trajectories, issued from an equal 'number of starting locations', $\mathrm{nsl}=T_j$, evenly distributed across the inlet jet section. Radial profiles of the normalized particle volume fraction are shown in Figure 6. These results, which were calculated using the same flow conditions for the carrier fluid, but with different values of nsl, illustrate that 4×10^4 particle trajectories ensure nearly stochastic independence. This number of particle injection points was thus adopted for the subsequent two-phase (fluid–particle) flow calculations.

Numerical predictions are presented next for both single-phase (fluid in the absence of particles) and two-phase (particle-laden fluid) flow conditions. The computed results are also compared with the corresponding laboratory measurements reported by Modarress *et al.* [31]. The inlet data in the experiments were obtained by these authors at $x=0.1D$, not exactly at $x=0$. However, in the numerical simulations, the inlet data must be prescribed at $x=0$, not at $x=0.1D$. Therefore an adjustment had to be introduced to compensate for this slight difference: the experimental inlet conditions at $x=0.1D$ were prescribed at $x=0$ in the numerical simulations; and then

DOI: 10.1002/fld

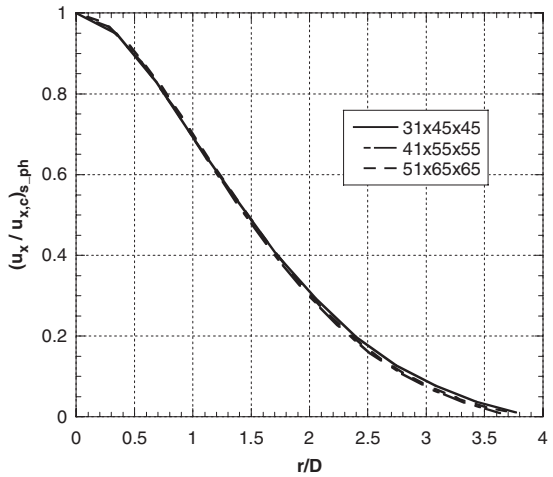

Figure 5. Normalized time-mean fluid velocity profiles (single-phase) calculated using different grids. $x/D=20$. $u_{x,c}$ is the value of u_x at the centerline.

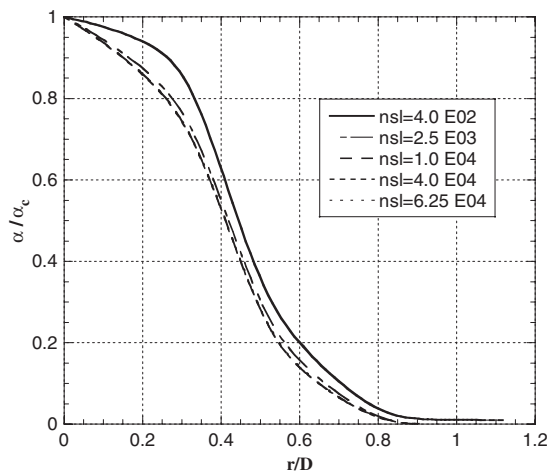

Figure 6. Normalized particle volume fraction profiles calculated using different values of nsl. $x/D=20$. α_c is the value of α at the centerline.

the experimental data of Modarress *et al.* [31] at $x/D=20$ was used to assess the numerical predictions obtained at $x/D=19.9$. Even though this adjustment was adopted in the present work, for simplicity and consistency with the experimental data of Modarress *et al.* [31] the longitudinal location $x/D=19.9$ in the numerical simulations will be denoted as $x/D=20$ in the presentation and discussion of the results in the following paragraphs and figures.

The predicted time-mean gas-phase streamlines and velocity vectors in the axial plane $y/D=7.5$ are presented in Figures 7 and 8. The streamlines in Figure 7 show that after entering the calculation domain, the co-flowing containment flow turns rather rapidly directed towards the jet axis in order

DOI: 10.1002/fld

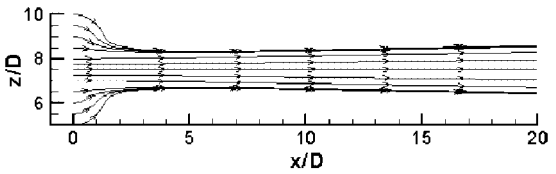

Figure 7. Predicted time-mean gas-phase streamlines in the axial plane $y/D=7.5$.

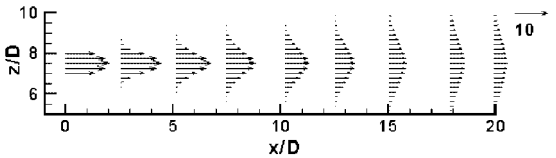

Figure 8. Predicted time-mean gas-phase velocity vectors in the axial plane $y/D=7.5$. The magnitude of the reference vector (upper right corner) is 10 m/s.

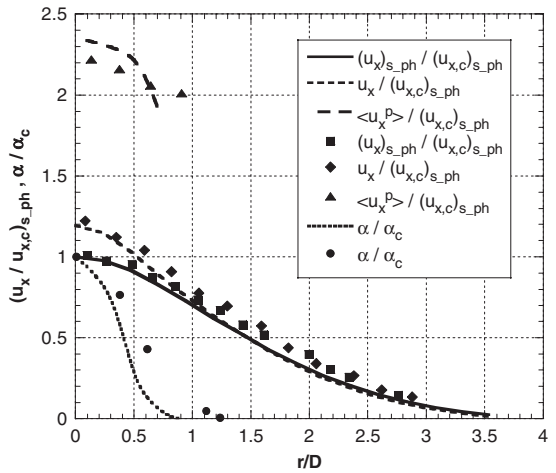

Figure 9. Predicted and measured radial profiles of normalized time-mean axial velocity and particle concentration, at $x/D=20$. Lines, present predictions; full marks, experiments.

to feed the jet entrainment. This entrainment of fluid into the jet is also evident at higher values of the longitudinal coordinate, x/D. The time-mean velocity vectors in Figure 8 also show the jet spreading for increasing values of x/D, which is in accordance with the information conveyed by the streamlines shown in Figure 7.

Predicted and measured radial profiles of the time-mean axial velocities are shown in Figure 9 for the single-phase flow (jet without particles), $(u_x)_{\mathrm{s\_ph}}$, and also for the fluid phase, u_x, and the particle phase, $\langle u_x^{\mathrm{p}}\rangle$, in two-phase flow conditions. These results pertain to the axial location $x/D=20$ and are normalized by the predicted, local centerline axial velocity of the single-phase flow, $(u_{x,c})_{\mathrm{s\_ph}}$. The calculated and the corresponding measured profiles are in excellent agreement

DOI: 10.1002/fld

for the single-phase flow and the fluid phase in two-phase flow conditions. Only fair agreement is observed for the particle-phase time-mean axial velocity radial profiles, where the differences between predictions and experiments tend to increase for increasing radial distances from the jet centerline. The influence exerted by the particles upon the fluid flow and *vice versa* (two-way coupling effect) can be assessed by comparing the radial profiles of time-mean axial velocity shown in this figure: the profile for the single-phase flow is different from that for the fluid flow in the two-phase case, due to the presence of particles; and this difference is clearly apparent in both the numerical and the experimental results. Furthermore, this difference is more pronounced in the region adjacent to the centerline than in the vicinity of the edge of the jet. Also displayed in Figure 9 is the radial profile of particle concentration, α (see Equation (19)), normalized by its centerline value, α_c. The measured concentrations become vanishingly small for higher radial distances than the calculated ones: even though the difference is not large, it probably means that the effect of fluid turbulence on particle dispersion is somewhat underestimated by the theoretical model of Equation (14). Although more elaborate alternatives are available to describe this effect, the 'particle–eddy dispersion model' of Gosman and Ioannides [27] was adopted in this work as it is still frequently used in practical applications because of its conceptual simplicity and easy implementation.

The effect of fluid turbulence on the dispersion of particles is clearly apparent through a comparison of the particle trajectories shown in Figure 10(a) and (b), where for the sake of clarity, only 25 starting locations (nsl = 25) were included. For the results presented in Figure 10(a), the turbulence dispersion of particles was accounted for through the particle–eddy dispersion model, whereas for those shown in Figure 10(b), the so-called *ballistic* approach (in which no turbulence dispersion is included) was used in the calculations.

The radial profiles shown in Figure 11 were predicted for the normalized time-mean axial velocity of the dispersed phase, at the axial location $x/D = 20$, with and without including the effect of fluid turbulence in the particle tracking procedure. In this latter case (rather crude, ballistic approach), the profile is slightly flatter in the region $0 \leqslant r/D \leqslant 0.5$, and there are virtually no particles outside the effective radial extent of the jet (here, for $r/D > 0.5$). Thus, based on the results provided in Figures 10 and 11, it may be concluded that in this demonstration problem, turbulent dispersion does, indeed, play a crucial role in the determination of the particle trajectories and velocity profiles.

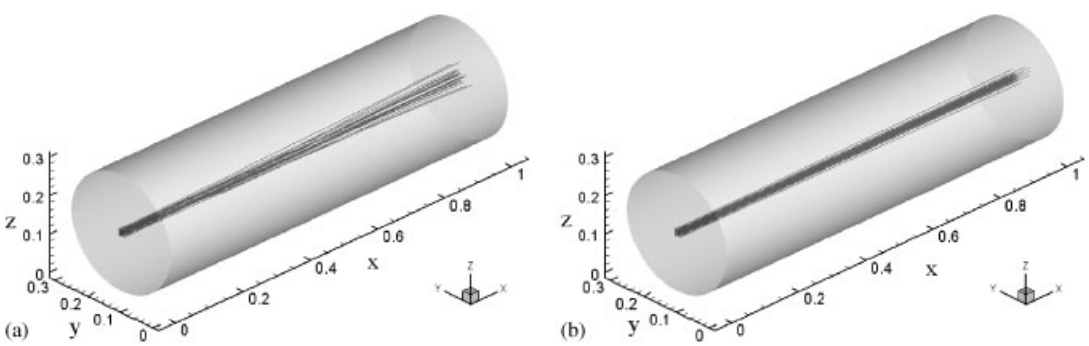

Figure 10. Predicted particle trajectories (nsl = 25), with (a) and without (b) inclusion of fluid turbulence on particle dispersion.

DOI: 10.1002/fld

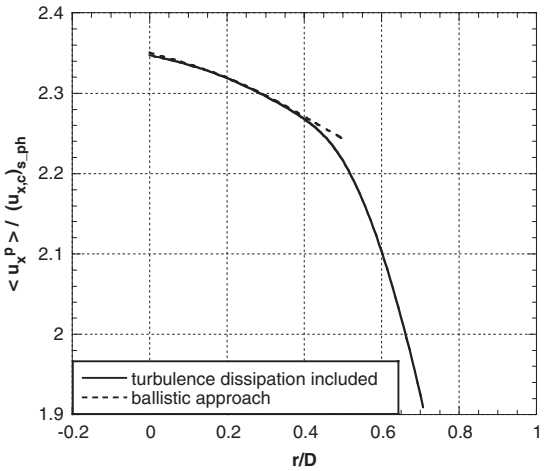

Figure 11. Predicted radial profiles of normalized time-mean axial velocity of the particle phase, at $x/D=20$, with and without inclusion of fluid turbulence in the calculation of particle trajectories.

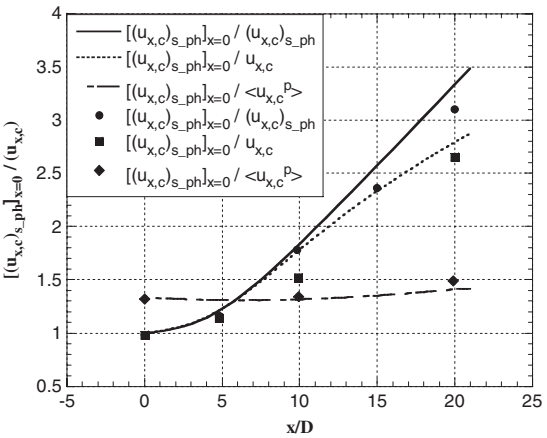

Figure 12. Axial evolution of centerline time-mean velocities, normalized by their values at $x=0$. Lines, present predictions; full marks, experiments.

The variation of the centerline time-mean axial velocities (single-phase flow $(u_{x,c})_{\mathrm{s\_ph}}$; fluid $u_{x,c}$, and particle $\langle u^{\mathrm{p}}_{x,c}\rangle$, in the two-phase flow) with the dimensionless streamwise coordinate, x/D, is shown in Figure 12. Here, the inverse of each centerline velocity is plotted, normalized with the single-phase time-mean centerline velocity at the jet origin, $[(u_{x,c})_{\mathrm{s\_ph}}]_{x=0}$. This latter reference velocity is equal to the fluid-phase time-mean centerline velocity at the same axial location, $(u_{x,c})_{x=0}$. The predicted fluid and particle centerline velocities reach an equilibrium condition with one another at a closer distance from the jet origin than those measured, but the overall agreement between the numerical and the experimental results is again quite satisfactory.

DOI: 10.1002/fld

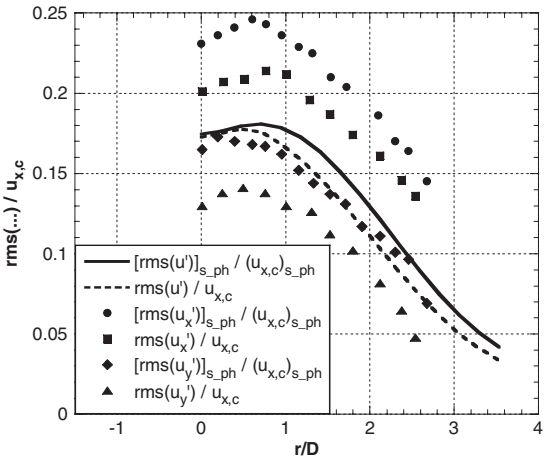

Figure 13. Predicted and measured radial profiles of turbulence intensity in the gas for the single-phase and the two-phase flows at $x/D=20$. Lines, present predictions; full marks, experiments.

In Figure 13, radial profiles of the following results at the axial station $x/D=20$ are presented for the gas in both the single-phase and the fluid–particle flows: the predicted values of the relative turbulence intensity, $\mathrm{rms}(u')/u_{x,c}=(\sqrt{2k/3})/u_{x,c}$; and the experimental values of $\mathrm{rms}(u'_x)/u_{x,c}$ and $\mathrm{rms}(u'_y)/u_{x,c}$ measured by Modarress *et al.* [13]. The considerable differences between the measured values of $\mathrm{rms}(u'_x)/u_{x,c}$ and $\mathrm{rms}(u'_y)/u_{x,c}$ at corresponding values of r/D are indicative of a considerable degree of turbulence anisotropy. The (isotropic) k–ε model used in this work for the prediction of the turbulent flow of the gas phase, in both the single-phase and the gas–particle flows, does not account for such turbulence anisotropy: this limitation of the present numerical approach could (at least in part) explain the discrepancy between the experimental and the predicted results. This finding suggests the need to use more sophisticated models of the turbulent flow of the gas phase, such as, perhaps, a suitable LES model. Additionally, the experimental results indicate that the turbulence intensity of the gas phase is attenuated by the presence of particles. This phenomenon of turbulence modulation is also evident in the numerical results, but under-predicted. Again, a more sophisticated turbulence model, such as an LES model, may improve the sensitivity of the fluid phase to this turbulence modulation effect of the particles.

In summary, the comparison established in this section between the predictions obtained with the present model for the demonstration problem and the corresponding experimental results may be considered satisfactory, especially in what concerns the time-mean transport in both single-phase (no particles) and two-phase (fluid–particle) flow conditions.

4. CONCLUSION

A numerical model for dilute, three-dimensional, turbulent, incompressible fluid–solid particle flows and its application to a demonstration problem have been presented in this paper. An Eulerian description was used to model the flow of the fluid (carrier) phase, and the governing equations were solved using a control-volume finite element method (CVFEM). The motion of the solid

DOI: 10.1002/fld

(particulate) phase was simulated using a Lagrangian approach. An efficient algorithm, already available for two-dimensional conditions, was extended for three dimensions and then successfully implemented for locating the particles in the finite element mesh.

In the demonstration problem, which involves a particle-laden axisymmetric jet, a modified k–ε turbulence model was used to characterize the velocity and length scales of the turbulent flow of the fluid phase. The effect of turbulence on the particle trajectories was accounted for through a relatively simple stochastic model. The effect of the particles on the fluid time-mean velocity and turbulence (two-way coupling) was also addressed. Comparisons between the predicted and the experimental results of Modarress *et al.* [13] for the selected demonstration problem showed satisfactory agreement.

ACKNOWLEDGEMENTS

This work was conducted under the research project entitled 'Local scale modelling of the flow dispersion of pollutant solid particles in complex geometry'—Bilateral Franco-Portuguese Cooperation Programme 'Pessoa' 2007/2008. The involvement of the third author was supported in part by a research grant from the Natural Sciences and Engineering Research Council (NSERC) of Canada.

REFERENCES

1. Crowe CT, Troutt, TR, Chung JN. Numerical models for two-phase turbulent flows. *Annual Review of Fluid Mechanics* 1996; **28**:11–43.
2. Crowe CT, Sommerfeld M, Tsuji Y. *Multiphase Flows with Droplets and Particles*. CRC Press: Boca Raton, FL, 1998.
3. Fan L-S, Zhu C. *Principles of Gas–Solid Flows*. Cambridge University Press: Cambridge, U.K., 1998.
4. Wilcox D. *Turbulence Modeling for CFD*. DCW Industries: La Canada, CA, 1993.
5. Ferziger HJ, Peric M. *Computational Methods for Fluid Dynamics*. Springer: Berlin, 1997.
6. Maliska CR, Raithby GD. A method for computing three-dimensional flows using non-orthogonal boundary-fitted coordinates. *International Journal for Numerical Methods in Fluids* 1984; **4**:519–537.
7. Shyy W, Tong SS, Correa SM. Numerical recirculating flow calculation using a body-fitted coordinate system. *Numerical Heat Transfer* 1985; **8**:99–113.
8. Karki KC, Patankar SV. Calculation procedure for viscous incompressible flows in complex geometries. *Numerical Heat Transfer* 1986; **14**:295–307.
9. Moukalled F, Acharya S. Improvements to incompressible flow calculation on a non-staggered curvilinear grid. *Numerical Heat Transfer* 1989; **15**:131–152.
10. Gresho PM, Sani RL. *Incompressible Flow and the Finite Element Method. Isothermal Laminar Flow*, vol. 2. Wiley: New York, 2000.
11. Reddy JN, Gartling DK. *The Finite Element Method in Heat Transfer and Fluid Dynamics* (2nd edn). CRC Press: Boca Raton, FL, 2000.
12. Zienkiewicz OC, Taylor RL, Nithiarasu P. *The Finite Element Method for Fluid Dynamics* (6th edn). Butterworth-Heinemann: Oxford, U.K., 2005.
13. Baliga BR. Control-volume finite element methods for fluid flow and heat transfer. In *Advances in Numerical Heat Transfer*, Chapter 3, vol. 1, Minkowycz WJ, Sparrow EM (eds), Taylor & Francis: New York, 1997.
14. Mathur SR, Murthy JY. Unstructured finite volume methods for multi-mode heat transfer. In *Advances in Heat Transfer*, Minkowycz WJ, Sparrow EM (eds). Taylor & Francis: New York, 2000; 37–70.
15. Baliga BR, Atabaki N. Control-volume-based finite-difference and finite-element methods. In *Handbook of Numerical Heat Transfer* (2nd edn), Chapter 6, Minkowycz WJ, Sparrow EM, Murthy JY (eds). Wiley: New York, 2006.
16. Murthy JY, Minkowycz WJ, Sparrow EM, Mathur SR. Survey of numerical methods. In *Handbook of Numerical Heat Transfer* (2nd edn), Chapter 1, Minkowycz WJ, Sparrow EM, Murthy JY (eds). Wiley: New York, 2006.
17. Oliveira LA, Costa VAF, Baliga BR. A Lagrangian–Eulerian model of particle dispersion in a turbulent plane mixing layer. *International Journal for Numerical Methods in Fluids* 2002; **40**:639–653.

DOI: 10.1002/fld

18. Oliveira LA, Costa VAF, Baliga BR. A Lagrangian model for the dispersion of solid particles, in three-dimensional flow, using a CVFEM for the prediction of the continuous phase. *Proceedings of RoomVent 2004, 9th International Conference on Air Distribution in Rooms*, University of Coimbra, Portugal, 5–8 September 2004.
19. Patankar SV. *Numerical Heat Transfer and Fluid Flow*. Hemisphere/McGraw-Hill: Washington, DC, 1980.
20. Costa VAF, Oliveira LA, Figueiredo AR. A control volume based finite element method for three-dimensional incompressible turbulent fluid flow, heat transfer, and related phenomena. *International Journal for Numerical Methods in Fluids* 1995; **21**:591–613.
21. Launder BE, Spalding DB. *Mathematical Models of Turbulence*. Academic Press: New York, 1972.
22. Pope SB. An explanation of the turbulent round-jet/plane-jet anomaly. *AIAA Journal* 1978; **16**:279–281.
23. Maxey MR, Riley JJ. Equation of motion of a small rigid sphere in a nonuniform flow. *Physics of Fluids* 1983; **26**:883–889.
24. Wallis GB. *One Dimensional Two-Phase Flow*. McGraw-Hill: New York, 1969.
25. Oliveira LA. Modelação Numérica da Dispersão de Partículas Sólidas no Escoamento de um Fluido: Conjugação de uma Estratégia Lagrangeana com o Método dos Elementos Finitos Baseado em Volumes de Controlo. *Proceedings of the Eventos do Centro Internacional de Matemática* (CIM), vol. 6, Escola de Elementos Finitos e Aplicações, University of Coimbra, Portugal, 22 September–2 October 1998 (paper no. 5).
26. Chen X-Q. Efficient particle tracking algorithm for two-phase flows in geometries using curvilinear coordinates. *Numerical Heat Transfer A* 1997; **31**:387–405.
27. Gosman AD, Ionnides E. Aspects of computer simulation of liquid fuelled combustors. *AIAA Paper No. 81–0323*, 1981.
28. Crowe CT, Sharma MP, Stock DE. The particle–source–in cell (PSI-CELL) model for gas–droplet flows. *Journal of Fluids Engineering* 1977; **99**:325–332.
29. Durst F, Milojevic D, Schönung B. Eulerian and Lagrangian predictions of particulate two-phase flows: a numerical study. *Applied Mathematical Modelling* 1984; **8**:101–115.
30. Gouesbet G, Desjonqueres P, Berlemont A. Eulerian and Lagrangian approaches to turbulent dispersion of particles. *International Seminars on Transition Phenomena in Multiphase Flow*, ICHMT, Dubrovnik, 1987.
31. Modarress D, Wuerer J, Elgobhashi S. An experimental study of a turbulent round two-phase jet. *Chemical Engineering Communications* 1984; **28**:341–354.
32. Elghobashi S, Abou-Arab T, Rizk M, Mostafa A. Prediction of the particle-laden jet with a two-equation turbulence model. *International Journal of Multiphase Flow* 1984; **10**:697–710.
33. Zhang Q-F, Shuen J-S, Solomon ASP, Faeth GM. Structure of diluted particle-laden turbulent jets. *AIAA Journal* 1984; **23**:1123–1125.
34. Aliud R, Dopaso C. Modelling and numerical computation of turbulent axisymmetric jets containing dilute suspensions of solid particles. *Proceedings of the 6th Symposium on Turbulent Shear Flow*, Toulouse, France, 7–9 September 1987; 21-2-1–21-2-7.

DOI: 10.1002/fld